Nuclear Materials and Energy 46 (2026) 102085

Contents lists available at ScienceDirect

Nuclear Materials and Energy

journal homepage: www.elsevier.com/locate/nme

Study on the influence of boronization on the first mirror unit in EAST

Zhaohui Wang [a,b], Rong Yan [a,b,*], Lei Mu [a], Yuming Liu [a,b], Chuannan Xuan [a,b], Yuxian Wen [a,b], Shuyue Sun [a,b], Guizhong Zuo [a], Rui Ding [a], Andrey Litnovsky [c], Junling Chen [a]

[a] Institute of Plasma Physics, Hefei Institutes of Physical Science, Chinese Academy of Sciences, Hefei 230031, Anhui, China
[b] University of Science and Technology of China, Hefei 230026, Anhui, China
[c] Forschungszentrum Jülich GmbH, Institute of Fusion Energy and Nuclear Waste Management (IFN-1), 52425 Jülich, Germany

ARTICLE INFO

Keywords:
Boronization
First mirror unit
Deposition
EAST

ABSTRACT

The new ITER baseline adopts full-tungsten (W) plasma-facing components (PFCs). Boronization is employed as the primary wall-conditioning technique to suppress oxygen (O) impurities during the initial operation stage. To evaluate its impact on diagnostic mirrors, a generic first mirror unit (FMU) mock-up was exposed to eight boronization cycles during the 2024 spring campaign in EAST. The FMU consists of the first mirror (FM), second mirror (SM), and third mirror (TM). These mirrors were protected by an aluminum (Al) baffle with a plasma-facing aperture adjacent to the FM. To better characterize the samples, each mirror in the FMU was composed of 16 small mirror samples. Reflectivity, surface morphology, and elemental composition were measured before and after exposure. The results revealed non-uniform deposition and varying degrees of reflectivity degradation across the three mirrors. Significant boron-based (B-based) layers were found only on the FM samples close to the aperture, exhibiting a symmetric spatial distribution consistent with the FMU geometry, with a thickness of approximately 200–400 nm. The B concentration reached up to ~30 at.%, leading to a maximum reduction of specular reflectivity from ~55% to ~1% at the wavelength of 380 nm. No obvious B-based deposits were detected on FM samples away from the aperture or on the SM and TM. However, these locations accumulated thin mixed films with thicknesses of several tens of nanometers, causing reductions of up to ~40 percentage points in specular reflectivity over 300–800 nm. All samples showed a pronounced increase in diffuse reflectivity, indicating a modification of the surface roughness. Given that each boronization typically produces ~100 nm of B-based coating on the first wall (FW) in EAST, these findings highlight the critical role and effectiveness of the baffle in mitigating direct deposition on diagnostic mirrors. Nevertheless, deposition induced by neutral particles during boronization and the re-deposition of sputtered FM material can still form non-uniform layers on the SM and TM, inevitably impairing their optical performance. These results provide important guidance for next-generation fusion devices, particularly regarding mirror protection, cleaning strategies, and reflectivity recovery.

1. Introduction

The first mirror (FM) is a critical component of optical diagnostics in next-generation fusion devices such as ITER and the Burning Plasma Experimental Superconducting Tokamak (BEST) [1,2]. Positioned to face the plasma directly, the FM is subjected to extreme conditions, including bombardment by energetic charge-exchange neutrals, re-deposition of sputtered plasma-facing materials (PFMs), and prolonged exposure to neutron and gamma irradiation [3,4]. These processes can cause surface sputtering or impurity deposition on the mirror surface. Sputtering may lead to the formation of micro relief or stepped structures [5], while impurity deposits may accumulate during plasma operation [6]. Both effects reduce the reflectivity of the FM, thereby degrading the accuracy and effectiveness of the associated optical signals. Single-crystalline (Sc) or nanocrystalline (Nc) materials can effectively mitigate the sputtering effect [5,7]. However, impurity deposits remain a critical challenge, as even thin deposition layers can cause absorption and interference effects, significantly reducing reflectivity in the ultraviolet (UV) and visible (VIS) ranges [8]. These deposits originate from first wall (FW) materials, such as beryllium (Be) deposits in JET with Be FW [9], carbon (C) deposits in DIII-D with graphite wall material [10], and from wall conditioning materials, such as lithium (Li)-containing deposits in EAST with routine Li coating [11].

In the JET tokamak with a C FW, C-based deposits exceeding 20 μm

* Corresponding author at: Institute of Plasma Physics, Hefei Institutes of Physical Science, Chinese Academy of Sciences, Hefei 230031, Anhui, China.
E-mail address: yanrong@ipp.ac.cn (R. Yan).

https://doi.org/10.1016/j.nme.2026.102085
Received 14 October 2025; Received in revised form 1 January 2026; Accepted 9 February 2026
Available online 12 February 2026

were observed on FM surfaces, reducing reflectivity by 80–90% [12]. Similar results were reported in DIII-D with a graphite FW [10,13]. After the upgrade to an ITER-like wall (JET-ILW) with a Be FW and W divertor, Be-based deposits were measured on FM surfaces, reducing reflectivity by 20–80% [14]. In the ASDEX Upgrade with full-W PFCs, some FMs were exposed for nearly nine months, with the highest reflectivity drop reaching –55% at 500 nm due to the deposits mainly containing W oxides and B [15]. Moreover, the Charge Exchange Recombination Spectroscopy (CXRS) mirror in EAST was covered with Li-based deposits due to routine Li wall conditioning. Reflectivity decreased from 71.4% to 15% at the wavelength of 532 nm after three experimental campaigns due to deposition [16]. Therefore, the development of deposition-mitigation methods and in situ cleaning strategies has become essential for ensuring the long-term reliability of optical diagnostics in ITER.

To mitigate impurity deposition on FM surfaces, shutters [16,17] and baffles [18,19] have been studied and proven effective. In the design of some first mirror units (FMUs), which provide the first optical deflection, such structures can be implemented to mitigate particle flow along the optical path [20]. Besides, radio frequency (RF) plasma cleaning [19] is considered one of the most promising technologies for removing deposition on FMs. Whether dealing with the Al/Al_2O_3 (simulating Be [21]) or W films coated in laboratories [22,23], RF plasma has exhibited robust cleaning capability. Furthermore, for the mixed deposited film formed during FM exposure experiments on tokamak devices such as EAST [16] and JET [24,25], RF plasma has similarly demonstrated excellent cleaning performance, with the reflectivity of the FMs largely restored. Recently, ITER has decided to change from Be FW to full-W FW. To achieve improved plasma performance, boronization has been adopted as a routine wall-conditioning technique. This baseline introduces new challenges for FM performance. Depositing a ~17 nm B film on a Mo FM via magnetron sputtering reduces its reflectivity from 60% to 10% at the wavelength of 460 nm [26]. However, studies on the impact of in situ boronization in tokamak environments on FM/FMU remain scarce. It is therefore essential to investigate how boronization affects FM/FMU behavior in tokamak environments. Such understanding is crucial for optimizing plasma cleaning solutions.

EAST is a fully superconducting tokamak equipped with W upper and lower divertors and a molybdenum-titanium-zirconium alloy (TZM, C 0.01–0.04 wt%, Ti 0.42–0.55 wt%, Zr 0.07–0.12 wt%, O $\leq$ 0.05 wt%) FW since 2021 [27,28]. Boronization using carborane ($C_2B_{10}H_{12}$) as the B source, assisted by ion cyclotron range of frequency (ICRF) discharge, has been applied in HT-7 and EAST [29,30]. Due to its ITER-like full-metal wall and boronization capability, EAST provides an ideal platform for studying the influence of boronization on the FMUs. In this paper, we present the first results from FMU mock-up exposures during boronization in EAST. Our focus lies in two main aspects: (1) the reflectivity behavior of mirrors within the FMU mock-up and (2) the distribution of deposits, particularly B, on the three mirrors. Section 2 describes the experimental setup, Section 3 presents results, Section 4 provides analysis and discussion, and Section 5 presents the summary and outlook.

2. Experimental setup

2.1. FMU preparation

The generic FMU mock-up used in this study comprised the FM, SM, and TM with identical dimensions (110 mm × 80 mm × 10 mm), as shown in Fig. 1. The FM and SM were mounted opposite each other, while the TM was positioned horizontally between them, forming angles of about 135° with the FM and 60° with the SM. Considering that the shutter may fail during operation and leave the mirror unprotected [31,32], it is essential to evaluate the FMU performance under such extreme conditions. For this reason, the generic FMU used in this study was equipped only with an integrated baffle. The end of the FM closer to the baffle was about 25 mm from it, while the far end was approximately 95 mm away. The baffle itself has a thickness of about 2.5 mm and directly faces the FM, containing an aperture of 65 mm × 70 mm to allow optical signals to pass. The light enters the FMU through the aperture on the baffle, is then sequentially reflected by the FM, SM, and TM, and finally exits through the same aperture.

To enable detailed characterization of the mirrors, 16 small mirror samples with dimensions of 27.5 mm × 20 mm × 5 mm were mounted on the FM, SM, and TM in a 4 × 4 array, as shown in Fig. 1. Direct fabrication of Mo mirrors with the required Nc structure and dimensions is not feasible. Therefore, TZM substrates were first precision-machined and then mechanically polished to obtain a mirror-like surface with a roughness (Ra) below 10 nm. The polished samples were subsequently ultrasonically cleaned for 15 min, first in high-purity ethanol and then in acetone. Finally, the polished substrate surfaces were coated with ~500 nm of Nc Mo as the reflective layer by magnetron sputtering. Coordinate systems were marked in red at the upper left corner of the FM, SM, and TM. The X direction was defined along the long edge, and the Y direction along the short edge. These coordinate systems were used to identify the positions of the small mirror samples. Besides, the generic FMU mock-up was exposed in the material and plasma evaluation system (MAPES)

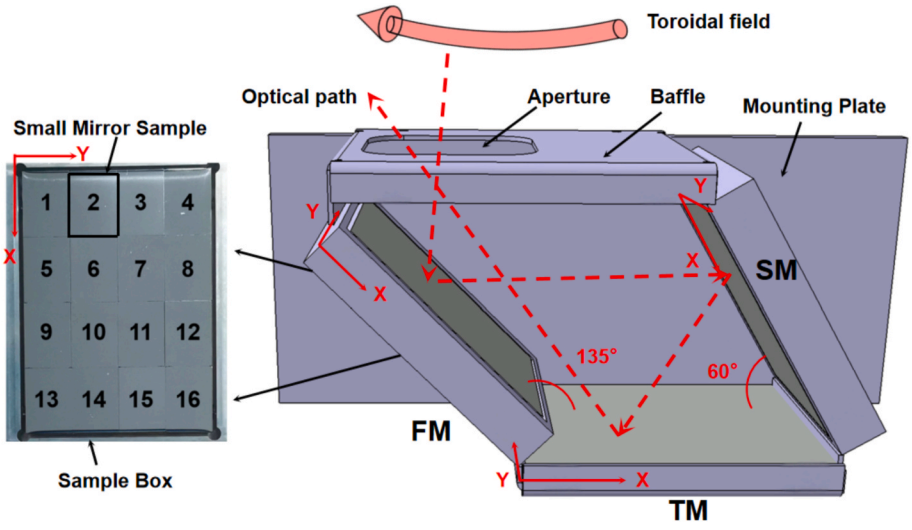

Fig. 1. Structure of the FMU and sixteen small mirror samples assembled on the FM. (The opposite mounting plate, which also holds the FMU at the center, is not shown to better illustrate the FMU structure.)

[33] in EAST. Owing to the limited load capacity of the MAPES system, both the baffle and the mounting plate were fabricated from a light-weight Al alloy to meet the safety requirements.

2.2. Boronization

During the 2024 spring campaign of the EAST tokamak, the FMU mock-up was mounted on the sample holder of MAPES. MAPES enables in-vessel sample transfer to the main scrape-off layer (SOL) at the mid-plane, as shown in Fig. 2. A total of eight boronization cycles were carried out, approximately once per week. After completing these cycles, the FMU was then removed. Following each boronization, the FMU was recessed into the MAPES independent chamber, far from the plasma. This ensured that the samples remained under vacuum and were well preserved between boronization cycles.

The first six boronization cycles employed D_2 ICRF plasma, whereas the final two used D_2 glow discharge (GD) plasma. ICRF-assisted boronization was carried out with a toroidal magnetic field of 0.5 T and a working pressure of 0.05 Pa. Two ICRF antennas, shown in Fig. 3, were used: one located between ports A and B (A–B) and the other between ports I and J (I–J). The A–B antenna operated at 30 kW, while the I–J antenna operated at 15–20 kW. GD-assisted boronization was performed without a magnetic field and at a higher pressure of 0.5 Pa. During the first GD-assisted boronization, three anodes were used, located at ports P–A, F–G, and J–K. In the final GD-assisted boronization, only two anodes at ports P–A and F–G were employed. In both GD-assisted cases, each anode maintained a consistent average power of ~400 W (2 A, 200 V).

The boronization procedure was as follows: D_2/He ICRF cleaning, lasting 0.5–3 h, was performed before boronization to reduce impurities, improve FW cleanliness, and enhance B film adhesion. Subsequently, B coating was conducted. The ovens were located at the midplane of ports F and O. $C_2B_{10}H_{12}$ was selected as the boronization material due to its low melting point (~370 K) and ease of sublimation. For each boronization, ovens containing 10 g of $C_2B_{10}H_{12}$ were placed in the vacuum vessel and gradually heated to 355–375 K. Once sublimated, the $C_2B_{10}H_{12}$ vapor was ionized by ICRF or GD plasma. After ionization, it was transported with or without the influence of the toroidal magnetic field and deposited on the FW surface. Complete evaporation required 1.5–2 h, after which the ovens were withdrawn.

A two-step post-treatment with ICRF or GD cleaning, lasting 0.5–2 h, was then performed. First, D plasma was applied to eliminate hydrogen from B–H co-deposited films. Next, He plasma was used to reduce residual deuterium and other gases retained in the wall. In total, 80 g of $C_2B_{10}H_{12}$ was consumed during the eight boronization cycles. The oven at port F operated for 10 h 50 min, while the oven at port O operated for 9 h 40 min.

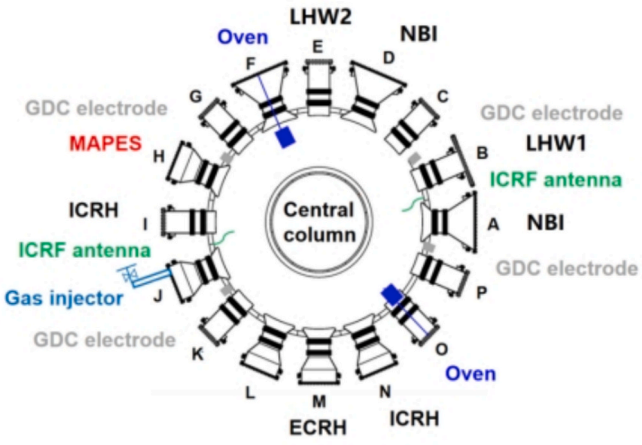

Fig. 3. Toroidal locations of the ovens, ICRF antennas, GDC electrodes, the gas inlet, auxiliary heating systems, and MAPES.

2.3. Samples characterization

The total and diffuse reflectivity of the small mirror samples were measured before and after exposure using an ultraviolet–visible-near-infrared spectrometer (Shimadzu 3700 DUV) within the wavelength range of 300–1200 nm. Based on the standard definition, the specular reflectivity was determined by subtracting the diffuse reflectivity from the total reflectivity. Besides, the reflectivity of Sample No.3 in the FM was measured at the University of Basel. The reflectivity–wavelength curves of all samples were nearly identical prior to exposure. Therefore, two representative small mirror samples from each large mirror were selected for further analysis. The specific samples chosen for detailed post-exposure characterization are shown in Fig. 4. Surface morphology was examined using a scanning electron microscope (SEM, Zeiss Sigma 300). The corresponding surface elemental composition was analyzed by energy-dispersive spectroscopy (EDS, Oxford X-MaxN). The EDS,

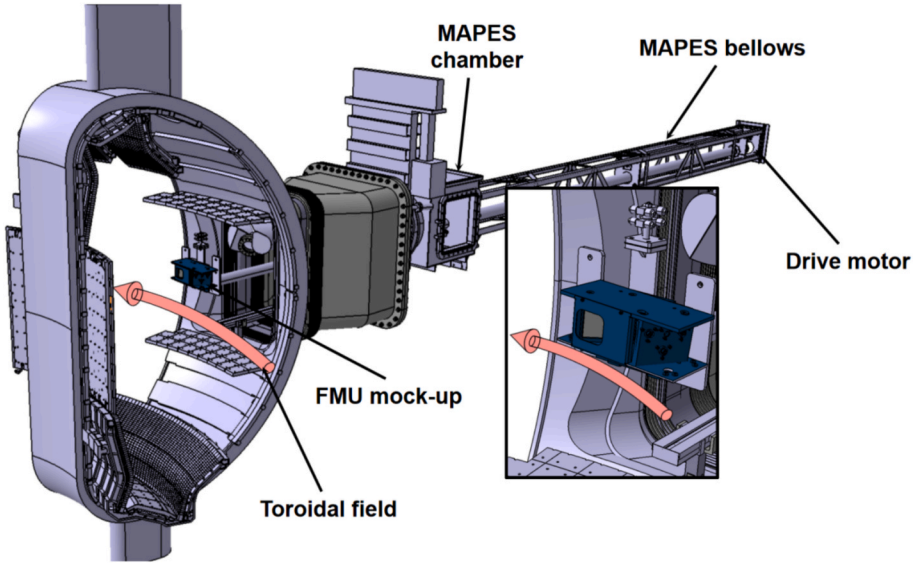

Fig. 2. Illustration of the FMU mock-up fixed on the MAPES manipulator and inserted in EAST.

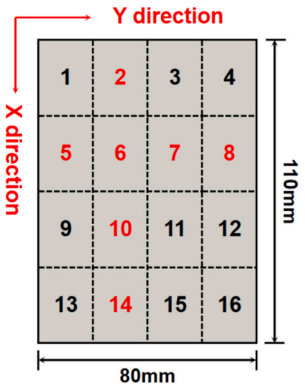

	FM	SM	TM
Reflectivity	1-16	1-16	1-16
SEM,EDS	2,5,6,7,8,10,14	2,5,6,7,8,10,14	2,5,6,7,8,10,14
XPS	2,6,10,14	2,6,10,14	2,6,10,14
FIB	2	2,10	6
SIMS	2	/	/

Fig. 4. Analyzed small mirror samples with locations measured by SEM, EDS, FIB, SIMS, and reflectivity.

integrated with the SEM, was operated at an electron beam energy of 5 keV. Given the shallow detection depth (~1 μm) of EDS and its limited sensitivity to trace elements, X-ray photoelectron spectroscopy (XPS, Thermo Scientific K-Alpha) was employed as a complementary method for surface elemental analysis. The thickness of B-based deposits was determined using a focused Ga^+ ion beam-scanning electron microscope (FIB-SEM, Helios G4 UX). For in-depth elemental distribution analysis, secondary ion mass spectrometry (SIMS) was carried out using a Bi^+ primary ion beam operated at an energy of 30 keV with a beam current of 1 pA. Elemental depth profiling was performed by successive sputtering of the surface using an O_2^+ ion beam. The total sputtering time was 412 s, corresponding to an effective sputtering rate of approximately 2.11 nm/s calibrated for SiO_2. The O_2^+ ion gun was operated at an acceleration voltage of 2 keV with an incident angle of 45° relative to the sample surface.

3. Results

3.1. Visual inspection

Pre- and post-exposure photographs of the FMU samples are presented in Fig. 5. The original small mirror samples (Fig. 5(a)) looked metallic, showing a clean surface with no visible contamination prior to exposure. After exposure, significant morphological changes were observed, as shown in Fig. 5(b–d). As shown in Fig. 5(b), the small mirror samples on the FM displayed multicolored surfaces outlined by dashed lines, covering about three-quarters of the FM. This appearance resulted from inhomogeneous deposits formed during exposure, similar to FM behavior in the JET device [34]. By contrast, the small mirror samples located far from the baffle aperture largely retained their metallic appearance, likely due to the shielding effect provided by the baffle. Unlike the FM, the SM (Fig. 5(c)) did not display multicolored patterns, but still exhibited zones of coloration delineated by dashed lines. These areas appeared darker than the surrounding surface and were separated from the unaffected regions by a distinct white, arc-shaped boundary. The TM shown in Fig. 5(d) differed markedly from both the FM and SM, remaining visually unchanged with no apparent color variations and maintaining a condition nearly identical to its pre-exposure state.

3.2. Reflectivity

To maintain clarity and avoid unnecessary complexity, the reflectivity wavelength data of the 16 small mirror samples on the FM were organized into three subsets according to their geometric locations. The corresponding specular reflectivity-wavelength curves are presented in Fig. 6(a–c), while the diffuse reflectivity results are shown in Fig. 6(d–f). The specular reflectivity of all FM samples exhibited a decrease, with the maximum reduction observed from ~55% to ~1% at the wavelength of 380 nm. In contrast, the diffuse reflectivity exhibited a substantial increase, attaining values in excess of 20% over some wavelength ranges. These trends suggest that boronization leads to a significant degradation of the optical performance of FM. Several small mirror samples demonstrated a high degree of similarity in their specular reflectivity-wavelength curves, corresponding to their symmetrical positions with respect to the Y = 40 mm axis of the FMU. For example, samples No.1 and No.4, as well as No.2 and No.3, showed comparable spectral behavior, as illustrated in Fig. 6(a–b). In addition, samples aligned along the Y direction (e.g., No.9–12 and No.13–16) displayed internal consistency within each group. These regularities indicate that the optical responses of the samples may be largely governed by their geometric locations in the FMU, where symmetric or colinear positions experience similar exposure conditions.

For the SM, as shown in Fig. 7(a–b), the specular reflectivity loss of the small mirror samples was most pronounced in the UV region, with some samples exhibiting reductions exceeding 50 percentage points. The loss in the VIS region was about 40 percentage points, while in the infrared (IR) region above 800 nm, the decrease of some samples was limited to about 20 percentage points. This pattern partially resembled the reflectivity changes observed in the FM. In contrast to the FM, the SM exhibited only two distinct types of specular reflectivity-wavelength curves. Samples No.1–4 in Fig. 7(a) displayed curves closely matching

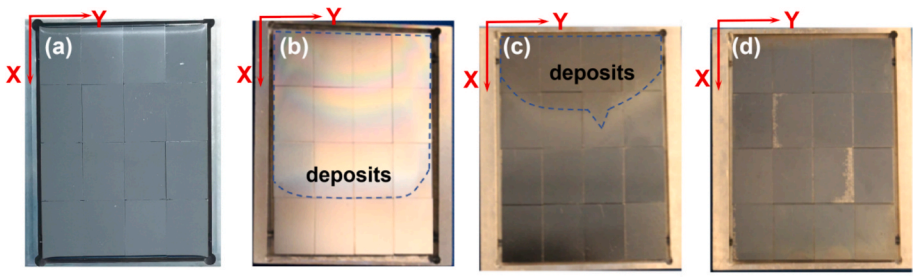

Fig. 5. Visual inspection of the FMU samples before and after exposure. (a) Original mirror; (b) FM after exposure; (c) SM after exposure; (d) TM after exposure.

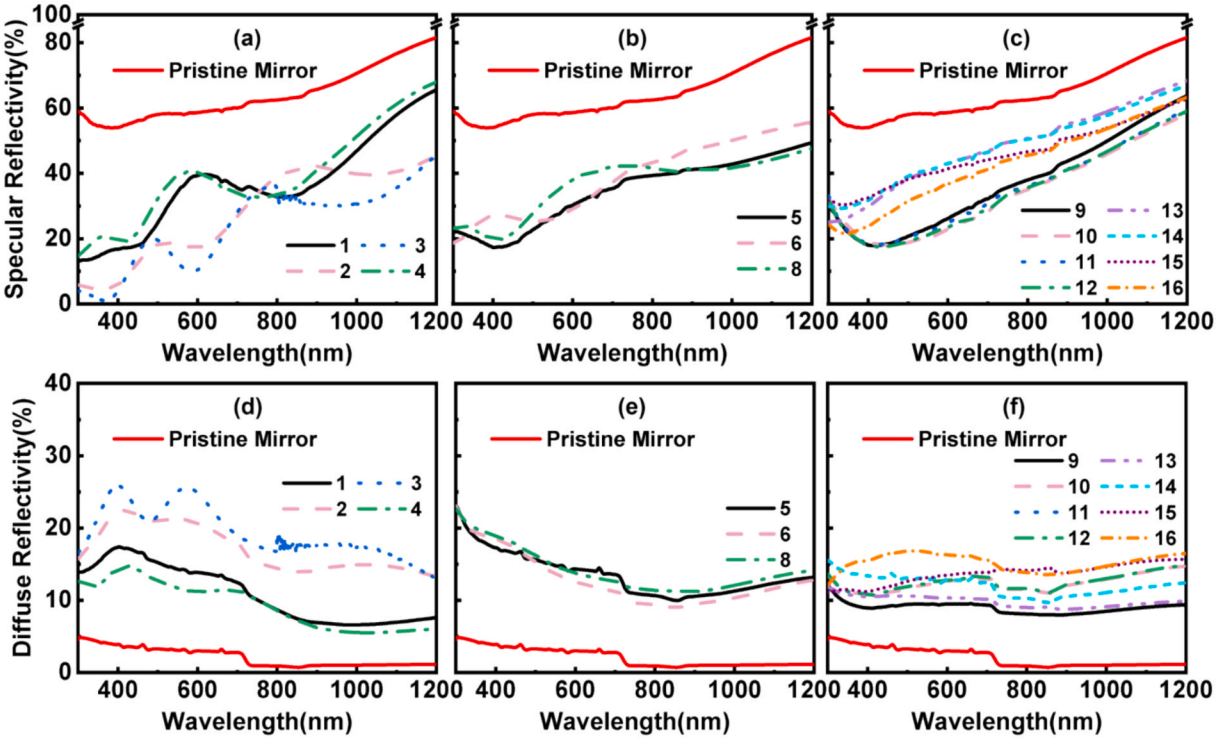

Fig. 6. Specular and diffuse reflectivity of small mirror samples on the FM after exposure: Specular reflectivity of samples (a) No.1–No.4, (b) No.5–No.8 and (c) No.9–No.16 Diffuse reflectivity of samples (d) No.1–No.4, (e) No.5–No.8 and (f) No.9–No.16.

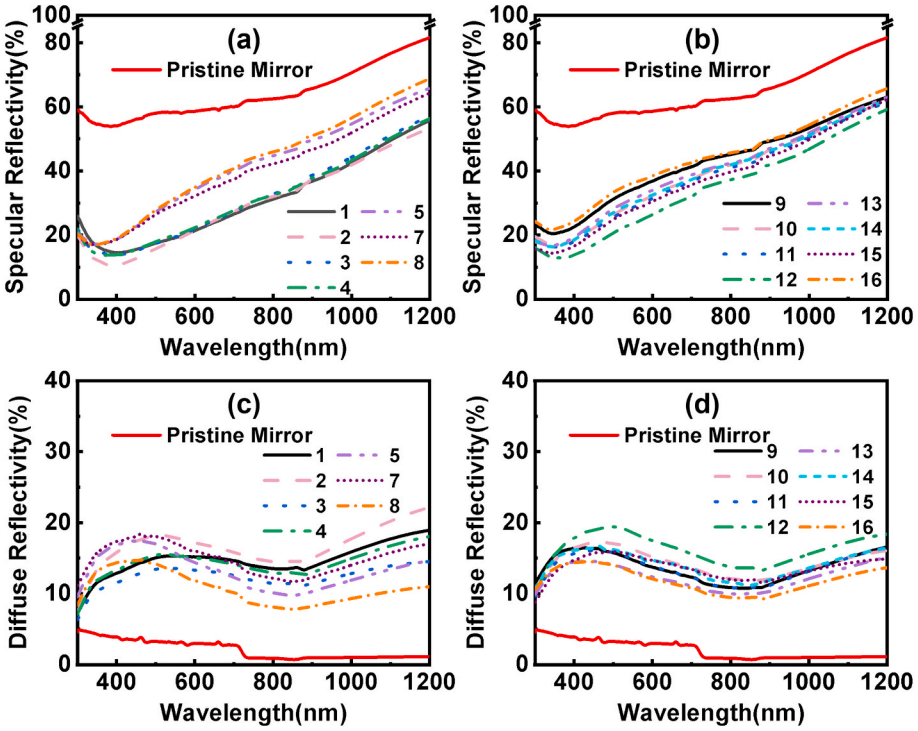

Fig. 7. Specular and diffuse reflectivity of small mirror samples on the SM after exposure: Specular reflectivity of samples (a) No.1–No.8 and (b) No.9–No.16. Diffuse reflectivity of samples (c) No.1–No.8 and (d) No.9–No.16.

those of FM samples No.9–12 in Fig. 6(c), whereas the remaining SM samples No.5–16 in Fig. 7(a–b) were more similar to FM samples No.13–16 in Fig. 6(c). In addition, Fig. 7(c–d) show that the diffuse reflectivity of several SM samples also increased noticeably.

As shown in Fig. 8(a–b), the specular reflectivity-wavelength curves of all samples on the TM are generally comparable to those of samples No.13–16 on the FM and No.5–16 on the SM, exhibiting similar trends. However, the TM samples located closer to the FM side (No. 1–8) exhibited a more pronounced reduction in specular reflectivity than those closer to the SM side (No. 9–16). Furthermore, consistent with the

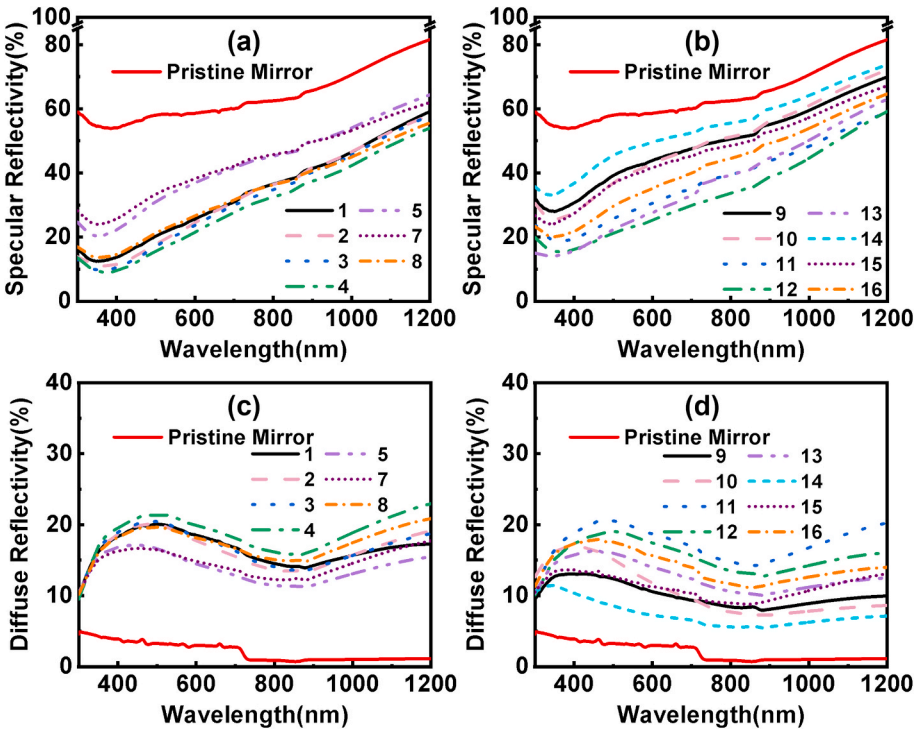

Fig. 8. Specular and diffuse reflectivity of small mirror samples on the TM after exposure: Specular reflectivity of samples (a) No.1–No.8 and (b) No.9–No.16. Diffuse reflectivity of samples (c) No.1–No.8 and (d) No.9–No.16.

observations on both the FM and SM, Fig. 8(c–d) show a clear increase in diffuse reflectivity across almost all TM samples. The degree of degradation also varied among individual samples. For example, sample No. 13 exhibited a loss in reflectivity exceeding twice that of sample No. 14, despite both samples showing similar overall specular reflectivity-wavelength trends.

4. Analysis and discussion

4.1. Elemental composition

4.1.1. Elemental composition of FM

Visual inspection clearly indicated that the deposition distribution on the FM closely correlated with the distance from the baffle aperture. EDS mapping scans were performed along both the longitudinal (X) and transverse (Y) directions of the FM, with the number of measurement points proportionally allocated according to the deposition pattern. The X and Y axes correspond to the positioning coordinates defined in Fig. 4, where the reference point is set at X = 0 and Y = 0. The relationship between elemental distribution and position is shown in Fig. 9. Along the X direction, the B concentration initially increased sharply to over 30 at.% at sample No.2, then gradually decreased, eventually dropping to 0 at.% at sample No.10. This trend can be attributed to the geometric position of the FM within the FMU mock-up. Positions near the edge of the baffle benefited from partial shielding, thereby reducing B concentration on the mirror. As the distance along the X direction increased, the region moved beyond the baffle's shielding zone and became exposed to the plasma. Consequently, the effect of boronization became more significant, leading to an initial rise in B content. With further increase in distance, the region moved progressively farther from the aperture. As a result, the influence of boronization diminished, and the atomic percentage of B gradually decreased. Beyond a certain point, the baffle regained its shielding effect due to the restricted aperture size, and B-based deposition was increasingly mitigated, eventually dropping to zero. Along the Y direction, the B concentration in the central region of the FM, such as No.7, reached up to ~15 at.%. This is higher than at the edges, such as No.8, where the concentration is approximately ~10 at. %, due to additional shielding of the peripheral areas by the baffle.

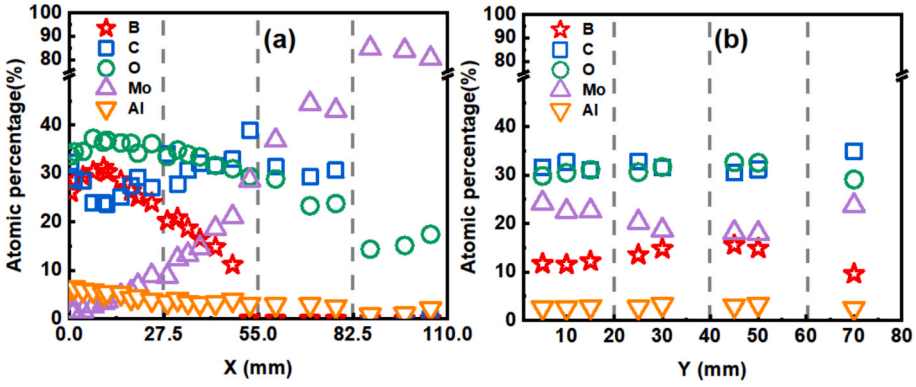

Fig. 9. Relationship between elemental distribution and distance (a) along the X direction; (b) along the Y direction in FM measured by EDS.

Interestingly, the B distribution was about symmetric with respect to the Y = 40 mm axis, suggesting a correlation between reflectivity symmetry and B content. Moreover, unlike along the X direction, elemental variation along the Y axis was minimal, indicating a more uniform deposition. This uniformity can be attributed to the approximately equal distance of all regions from the aperture. In both the X and Y directions, a certain amount of Al was detected. Since Al is not a PFM in EAST, it likely originates from the Al-alloy baffle of the FMU mock-up via sputtering and re-deposition. Given the limited sensitivity of EDS, complementary XPS analyses were conducted to provide more accurate compositional information. These results are summarized in Table 1. XPS analysis revealed the presence of B and C in all the examined samples. Even in samples where EDS detected no B or C (e.g., FM-14), XPS still identified ~10 at.% B and ~20 at.% C.

4.1.2. Elemental composition of SM and TM

As described in Section 3.1, visual inspection of the SM revealed three distinct regions: a heavily colored deposition area, a lighter-colored non-depositional area, and a white crescent-shaped boundary separating the two. EDS results indicated that along the X direction of the SM, C concentrations of up to ~30 at.% were detected in the darker deposition region, whereas no C was detected in the other two regions, as shown in Fig. 10(a). This finding suggests a strong correlation between deposition on the SM and the presence of C. Along the Y direction, EDS mapping scans were performed at the white crescent-shaped boundary between the deposition and non-depositional regions, as shown in Fig. 10(b). No C was detected in this region; only O, Al, and Mo were identified, with negligible compositional variation. For the TM, as illustrated in Fig. 10(c–d), the results show a clearer pattern. EDS scans along both the X and Y directions detected O, Al, and Mo with only small variations. It is noteworthy that EDS did not detect B on either the SM or TM. However, the XPS results in Table 1 revealed about 10 at.% B and 20 at.% C on the surface of these samples. It could be deduced that a thin mixed deposit containing B, C, O, and Al formed on the surface of SM and TM. Such thin deposits are responsible for the reduced reflectivity observed on both the SM and the TM.

4.2. Microscopic inspection

Several representative locations on the FM (b–e) were selected for microscopic inspection characterization, as shown in Fig. 11. Fig. 11(a) shows the Nc Mo surface before exposure, which exhibited a relatively homogeneous striped structure [22]. EDS mapping indicated B concentrations of ~30, 20, 10, and 0 at.% at locations (b)–(e), corresponding to small mirror samples No.2, 6, 8, and 10 (in Fig. 4). These locations spanned different distances from the baffle aperture, allowing a systematic comparison of spatial variations. From location (b) to (e), the FM surface evolved from being dominated by dense B-based particles near the aperture to a morphology increasingly similar to the pristine substrate farther away. Besides, as shown in Fig. 11(b), the B-rich particles progressively aggregated into interconnected branched-chain structures as the local B content increased [35]. Near the aperture (location b), dense B-based deposits covered most of the surface, while locations farther from the aperture experienced stronger baffle shielding, resulting in fewer B-based deposits. Non-uniform deposition resulted in variations in film thickness, which may lead to the formation of cracks, as illustrated by the red arrows in Fig. 11(b–c). On the SM and TM, deposits were significantly fewer, and their overall surface morphology exhibited relatively high similarity. Therefore, the surface morphology at location (f) on the No.2 small mirror sample in the SM was selected as representative for analysis, as shown in Fig. 11(f). In this location, no dense B-based particles or branched-chain structures were observed. However, some impurity particles similar to those on the FM were present. These particles contained elements such as iron (Fe) and Si, which originated from sputtered and re-deposited materials from the FW and other EAST components [16]. Most regions exhibited a thin and uneven film, which formed step-like structures in specific areas. Small white particles were also found on the FM, SM, and TM, and EDS identified them as Al and its oxides. These oxidized Al particles are consistent with the widespread presence of Al detected in the elemental composition section.

Table 1
Elemental composition measured by XPS at different small mirror samples.

Number	X (mm)	Y (mm)	B (at. %)	C (at. %)	O (at. %)	Al (at. %)	Mo (at. %)
FM-2	14	30	46	18	27	8	1
FM-14	96	30	9	24	43	14	10
SM-6	41	30	15	23	41	8	13
SM-10	69	30	9	25	42	8	16
TM-2	14	30	9	26	41	6	18
TM-6	41	30	6	28	36	9	21
TM-10	69	30	8	26	40	6	20

4.3. Depth distribution of deposits

Depth distribution analysis of the FM primarily focused on the No.2 small mirror sample shown in Fig. 4. Three locations were examined by FIB-SEM, with results summarized in Table 2. All measurements on the FM showed that the deposited film was below 400 nm, which is significantly thinner than the micron-scale film reported in some irradiation experiments [12,16]. This difference primarily arises from variations in exposure duration and specific experimental conditions. The deposition thicknesses of the SM and TM are also listed in Table 2. For the SM, two locations were selected: one within the visually identifiable deposition region and another in a visually clean area. Since no visible deposition was observed on the TM, a single location was randomly chosen for analysis. The results confirmed the presence of a deposited film on both mirrors. Moreover, even when considering the measurement uncertainty of FIB-SEM, the deposition thicknesses on the SM and TM are significantly lower than those on the FM. The deposition distribution was also highly non-uniform, exhibiting notable thickness variations. These findings are consistent with the uneven film morphology observed in Fig. 11(f). Analysis of the deposition thicknesses further emphasizes the role of the baffle in mitigating deposition within the FMU. Under typical EAST conditions, a single boronization produces a B film of ~100 nm on the FW [35]. However, after eight consecutive boronization cycles, the B-based deposited film on the FM remained below 400 nm in this study, even in the region with the highest accumulation. This thickness is still far lower than the theoretical estimate of ~800 nm. Due to the direct shielding provided by the baffle, the deposits on the SM and TM were even thinner, both remaining below 100 nm. These results indicate that, even under the adverse scenario in which the active shutter fails, the integrated baffle is still capable of attenuating the incident particle flux. As a result, it effectively mitigates deposition on all three mirrors inside the FMU including the FM, which is directly exposed to the baffle aperture.

In addition, SIMS analysis was performed to evaluate elemental distribution within the deposited layer on the FM, with results shown in Fig. 12. The analysis revealed a gradual decrease in the signal intensity of all elements except Mo with increasing depth. This trend occurs because, as depth increases, the analysis approaches the Nc Mo substrate. When combined with EDS analysis, the results confirm that B is a major component of the deposited film, indicating significant B accumulation on the FM during boronization. Furthermore, the depth profiles of elemental signals showed consistent behavior, with B and C exhibiting correlated trends. This correlation indicates that B deposition was typically accompanied by C, which is expected since the boronization material $C_2B_{10}H_{12}$ contains a substantial amount of C. Consequently, the deposition behaviors of these two elements are closely linked. Although Al and B exhibited relatively strong signals compared with other elements, this does not directly reflect their true abundance

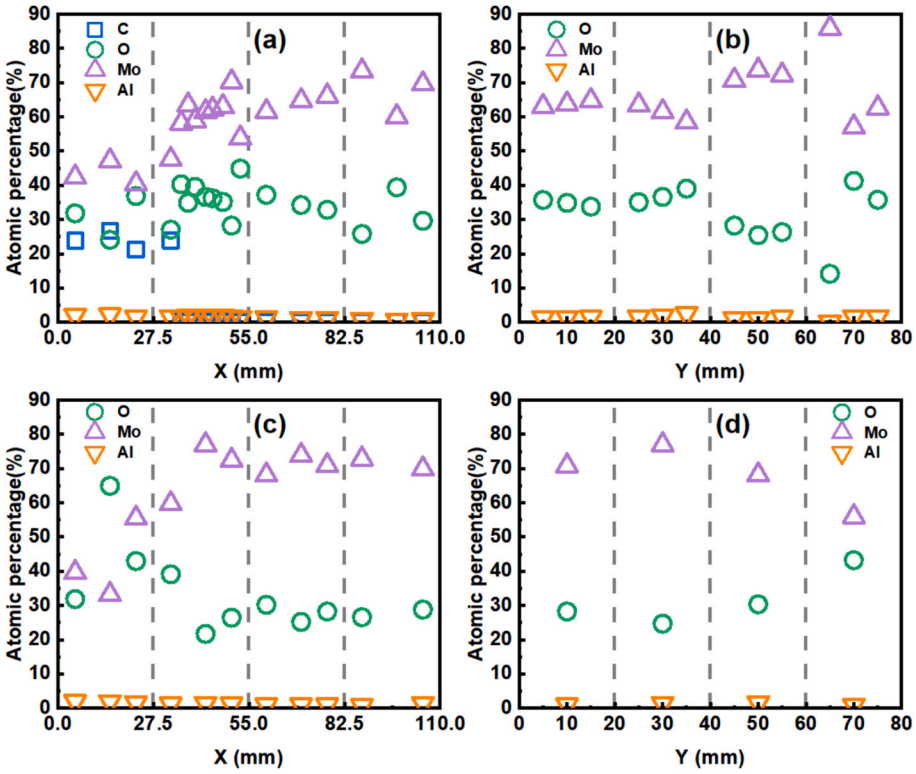

Fig. 10. Relationship between elemental distribution and distance (a) along the X direction in SM; (b) along the Y direction in SM; (c) along the X direction in TM; (d) along the Y direction in TM measured by EDS.

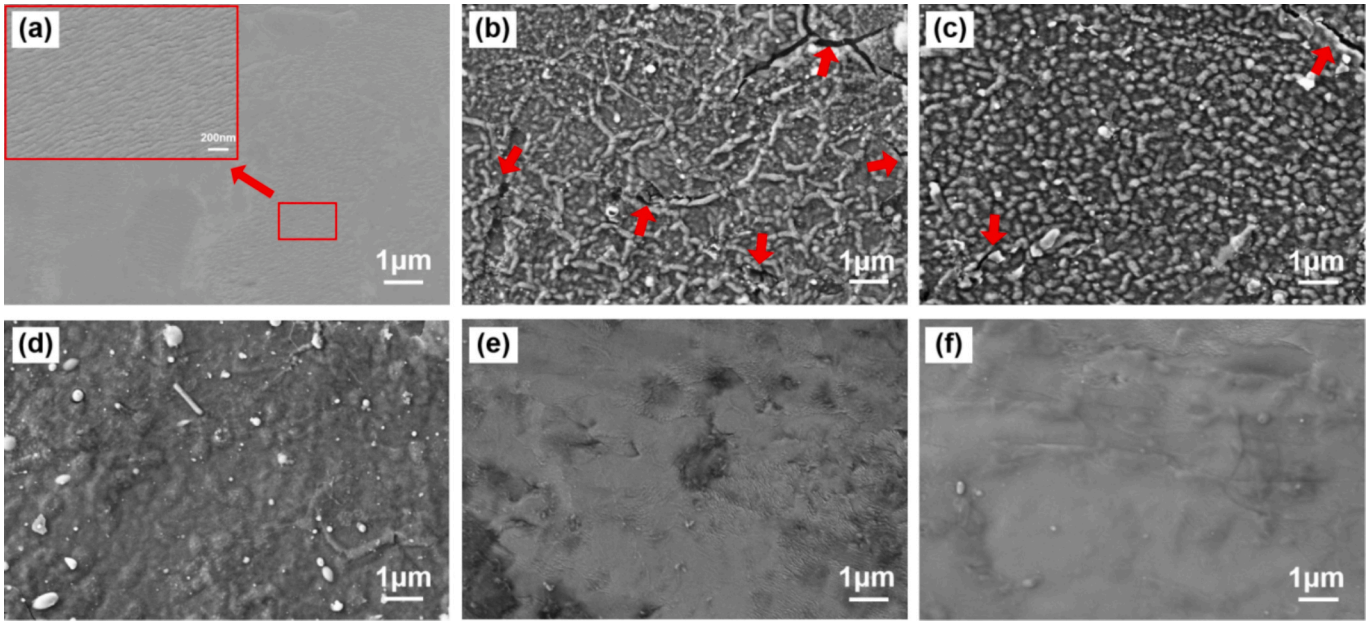

Fig. 11. SEM of the small mirror sample: (a) before exposure; (b) FM location with 30 at.% B; (c) FM location with 20 at.% B; (d) FM location with 10 at.% B; (e) FM location with 0 at.% B; (f) SM location with 0 at.% B. (B concentrations obtained by EDS.)

in the deposits. The SIMS signal intensity strongly depends on the sputtering yield of each element under ion bombardment, which can differ by several orders of magnitude. Therefore, elemental concentrations cannot be directly deduced from signal intensities alone [36]. This explains the discrepancies between SIMS and EDS results.

4.4. Discussion

Given the correlation between reflectivity variations and deposition, the above analyses suggest that the observed reflectivity changes may be related to the deposition [37]. Boronization exerted the most significant impact on the No.1–8 small mirror samples in the FM, which were largely unshielded by the baffle, leading to the formation of B-based

Table 2
Film thickness at different positions on different mirrors (measured by FIB-SEM).

Number	X (mm)	Y (mm)	Film thickness, measurement 1 (nm)	Film thickness, measurement 2 (nm)	Film thickness, measurement 3 (nm)	Average thickness (nm)
FM-2	2	30	322	378	385	362
FM-2	4	30	301	252	280	278
FM-2	25	30	220	231	203	217
SM-2	14	30	57	74	50	60
SM-10	69	30	29	46	96	57
TM-6	41	30	15	57	41	38

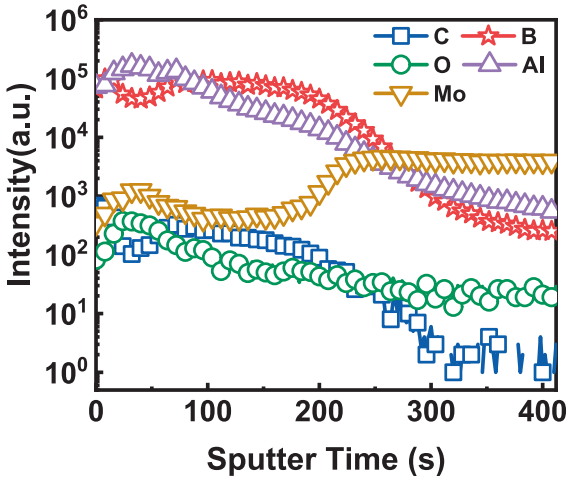

Fig. 12. Depth profiles of different elements in the FM analyzed by SIMS.

deposited film ~300 nm thick and consequently causing a pronounced reduction in reflectivity. However, differences in sample distances from the aperture, combined with the variable shielding effect of the baffle (with side samples receiving more shielding than those at the center), resulted in variations in B content. As discussed in Section 4.2, B may exhibit aggregation behavior; therefore, the surface morphology of the B-based deposition layer differed markedly with varying atomic B contents. These morphological differences may lead to varying degrees of reflectivity degradation among those small mirror samples [37]. Compared with some previous studies [10–15], the present results with B-based deposits in the range of ~300 nm and reflectivity losses of up to 60 percentage points, indicate that boronization also represents a critical threat to FM performance. Besides, the reflectivity-wavelength curves exhibited approximate symmetry along the Y = 40 mm line. This is likely related to the symmetric deposition pattern determined by the geometric arrangement of the FMU and the shielding effect of the baffle. During boronization, both ionized and neutral particles are present [38]. Ionized $C_2B_{10}H_{12}$ follows magnetic field lines, while neutral particles which are not constrained by the magnetic field, can reach a wider range of locations. Considering the installation position of the FMs and the actual arrangement of the FMU mock-up in this experiment, the B-based deposits are more likely due to neutral particle transport [39,40] though contributions from ionized particles cannot be entirely excluded. The baffle further modulates the deposition pattern, producing an approximately symmetric distribution of B content around the Y = 40 mm axis, as shown in Fig. 9(b). Variations in B content subsequently affected surface morphology, providing a reasonable explanation for the observed symmetry in reflectivity.

In addition to direct boronization effects on the FM, re-deposition within the FMU structure also played an important role. For the No.9–12 small mirror samples in the FM, although EDS did not detect B-based deposits, substantial amounts of C-based deposits were observed. The reflectivity variations of these samples are therefore primarily associated with C, such as carbides or a-C:H, as reported in [41,42], as well as those of with No.1–4 small mirror samples in the SM. Moreover, based on the geometric positions of the FM and SM within the FMU mock-up, it is reasonable to hypothesize that the C detected on the SM originated from sputter re-deposition on the FM. For all remaining small mirror samples, including No.13–16 in the FM, No.5–16 in the SM, and all samples in the TM, the reflectivity-wavelength curves exhibited highly consistent trends. The above results indicate that a thin mixed deposit containing B (~10 at.%) and C (~20 at.%) formed on the surfaces of these small mirror samples. This mixed deposit is responsible for the observed reflectivity decrease on the SM and TM. Previous studies have shown that even very thin films (10–30 nm) [8,22,26] can significantly reduce mirror reflectivity. This reduction is caused by absorption of incident light and destructive interference effects arising from uneven film thickness. Besides, the observed variation in reflectivity loss is thus governed by the thickness and composition of the mixed deposited film [8]. Considering the actual position of the FMU during the experiment, the deposits on the SM and TM may originate from neutral particle deposition during boronization and may also come from deposition sputtered from the FM and subsequently re-deposited within the FMU. In addition to specular reflectivity, these deposits also affected the diffuse reflectance of the mirror surfaces. The formation of mixed films increased surface roughness and local thickness non-uniformity. The results further indicate that the boronization process contributed to the overall optical degradation of the FMU.

5. Summary and outlook

The exposure of the generic FMU mock-up during boronization in EAST with an ITER-like wall configuration revealed several noteworthy results:

Under adverse conditions where the active shutter is unavailable or fails, the baffle effectively mitigates particle flux and mitigates deposition growth. However, neutral particles can enter through the aperture and affect the FM, which directly faces the aperture, resulting in localized deposition and reduced reflectivity. In addition, different boronization techniques, such as ICRF-assisted boronization and GD-assisted boronization, exhibit different particle-migration characteristics because of the presence or absence of a confining magnetic field. As a result, their abilities to limit particle flux are not the same, which may lead to different deposition behaviors and mirror degradation in the FMU. Further experiments are therefore required to systematically assess how these boronization methods influence deposition patterns and optical performance. Moreover, in ITER and future fusion devices, the FMU will experience both boronization and plasma discharges over long-term operation. Future experiments will also investigate their combined effects on mirror surfaces to better understand reflectivity evolution under realistic conditions.

Re-deposition within the FMU was also observed. In EAST, carborane is used for boronization instead of the diborane foreseen for ITER, so C is intrinsically introduced into the deposition environment. As a result, the C-containing films observed on the FM and SM can be interpreted as re-deposited film formed from sputtered materials in this C-rich boronization condition, which in turn leads to a noticeable decrease in mirror reflectivity. In future ITER-relevant studies, where diborane will be used and no intentional C is introduced, the impact of boronization-induced deposition on mirror performance can be investigated without the

additional contribution from C. Al was detected on all three mirrors with a relatively uniform distribution, indicating sputtering from the baffle components. As one of the major compositions of the deposited film, Al also plays a role in reflectivity loss. To distinguish the roles of these different deposition pathways and to obtain ITER-relevant results, future experiments will employ stainless-steel baffles and diborane boronization. Besides, for BEST and other machines in future, we think it is still meaningful to consider other structural material options such as W.

In summary, the results demonstrate that although the baffle substantially mitigates direct deposition, sputtering and re-deposition inside the FMU can still influence mirror surfaces and their reflectivity. Differences in film thickness among the mirrors were also identified. These findings highlight the difficulty of maintaining mirror performance, as both cleaning and reflectivity recovery are hindered by the persistent formation of mixed deposited layers. At the same time, they provide a practical basis for improving deposition control and developing more effective mitigation strategies for future applications.

CRediT authorship contribution statement

Zhaohui Wang: Writing – original draft, Methodology, Investigation, Data curation, Conceptualization. **Rong Yan:** Writing – review & editing, Supervision, Project administration, Methodology, Funding acquisition. **Lei Mu:** Methodology, Investigation. **Yuming Liu:** Writing – review & editing, Methodology, Investigation, Data curation. **Chuannan Xuan:** Writing – review & editing, Methodology. **Yuxian Wen:** Methodology, Data curation. **Shuyue Sun:** Methodology, Data curation. **Guizhong Zuo:** Methodology, Data curation. **Rui Ding:** Writing – review & editing, Data curation. **Andrey Litnovsky:** Writing – review & editing, Methodology. **Junling Chen:** Resources, Project administration, Funding acquisition.

Declaration of competing interest

The authors declare that they have no known competing financial interests or personal relationships that could have appeared to influence the work reported in this paper.

Acknowledgments

This work was supported by the National key R&D project of China with project number of 2024YFE03000200, 2022YFE03030000, the National Nature Science Foundation of China under Contract Nos. 12522515, 12275306, 11975269, U24A2020, and 12075279, the Youth Innovation Promotion Association of Chinese Academy of Sciences under certificate No. 2022452, the Anhui Provincial Natural Science Foundation under contract No. 2208085 J40, the Anhui Provincial Major Science and Technology Project under contract No. E35AH205B3, the CASHIPS Director's Fund with Grant Nos. BJPY2023B03, YZJJQY202302 and BJPY2023A03, and the Comprehensive Research Facility for Fusion Technology Program of China with grant No.2018-000052-73-01-001228.

We thank the staff members at EAST (https://cstr.cn/31130.02.EAST), for providing technical support and assistance in experiment, data collection, and analysis. We also acknowledge Prof. L. Marot from the University of Basel for helping measure the reflectivity of some samples and providing data analysis support.

Appendix

Abbreviation	Full Name	Abbreviation	Full Name
FM	First Mirror	SM	Second Mirror
TM	Third Mirror	FMU	First Mirror Unit
UV	Ultraviolet	VIS	Visible
IR	Infrared	PFCs	plasma facing components
Sc	Single-crystalline	Nc	Nano-crystalline
FW	First Wall	PFM	plasma-facing material
BEST	Burning Plasma Experimental Superconducting Tokamak	EAST	Experimental Advanced Superconducting Tokamak
CXRS	Charge Exchange Recombination Spectroscopy	RF	Radio Frequency
Ra	Roughness	ICRF	Ion Cyclotron Range of Frequency
MAPES	Material and Plasma Evaluation System	TZM	Molybdenum-titanium-zirconium
GD	Glow Discharge	SOL	Scrape-Off Layer
SEM	Scanning Electron Microscope	EDS	Energy-Dispersive Spectroscopy
XPS	X-ray Photoelectron Spectroscopy	FIB-SEM	Focused Ion Beam-Scanning Electron Microscope
SIMS	Secondary Ion Mass Spectrometry		

Data availability

Data will be made available on request.

References

[1] K. Soni, S. Iyyakkunnel, R. Steiner, et al., Effect of 3 T magnetic field on RF plasma sputtering in an ITER-relevant first mirror unit, Nucl. Fusion 62 (2022) 126009.
[2] EUROfusion, BEST Research Plan v1.1, November 2025, [Online]. Available: https://euro-fusion.org/wp-content/uploads/2025/11/BEST-Research-Plan-v1.1.pdf.
[3] E. Mukhin, V. Semenov, A. Razdobarin, et al., First mirrors in ITER: material choice and deposition prevention/cleaning techniques, Nucl. Fusion 52 (2011) 013017.
[4] B. Kim, K. Chai, J. Park, et al., Erosion resistance test of SiC mirror sample for ITER divertor VUV spectrometer, Fusion Eng. Des. 200 (2024) 114210.
[5] V. Voitsenya, A. Bardamid, A. Donné, et al., Experimental simulation of the behaviour of diagnostic first mirrors fabricated of different metals for ITER conditions, Open Phys. J. 3 (2016) 23–54.
[6] V. Voitsenya, A. Costley, V. Bandourko, et al., Diagnostic first mirrors for burning plasma experiments (invited), Rev. Sci. Instrum. 72 (1) (2001) 475–482.
[7] F. Sanchez, L. Marot, R. Steiner, et al., Surface modification of ITER-like mirrors after one hundred cleaning cycles using radio-frequency plasma, J. Nucl. Mater. 581 (2023) 154382.
[8] V. Bondarenko, W. Fukarek, V. Konovalov, et al., Effect of thin film goating on reflectance of in-vessel metallic mirror, J. Plasma Fusion Res. SERIES 3 (2000) 270–273.
[9] D. Ivanova, M. Rubel, A. Widdowson, et al., An overview of the comprehensive first mirror test in JET with ITER-like wall, Phys. Scr. T159 (2014).
[10] A. Litnovsky, D. Rudakov, G. Temmerman, et al., First tests of diagnostic mirrors in a tokamak divertor: an overview of experiments in DIII-D, Fusion Eng. Des. 83 (1) (2008) 79–89.
[11] P. Jiao, R. Yan, J. Chen, et al., Study on plasma cleaning of the large-scale first mirror of the charge exchange recombination spectroscopy diagnostic on EAST, Plasma Sci. Technol 22 (2019) 034004.
[12] M. Rubel, D. Ivanova, J. Coad, et al., Overview of the second stage in the comprehensive mirrors test in JET, Phys. Scr. T145 (2011).
[13] D. Rudakov, C. Wong, A. Litnovsky, et al., Overview of the recent DiMES and MiMES experiments in DIII-D, Phys. Scr. T138 (2009).
[14] S. Moon, P. Petersson, M. Rubel, et al., First mirror test in JET for ITER: complete overview after three ILW campaigns, Nucl. Mater. Energy 19 (2019) 59–66.

[15] A. Litnovsky, M. Matveeva, A. Herrmann, et al., First studies of ITER-diagnostic mirrors in a tokamak with an all-metal interior: results of the first mirror test in ASDEX Upgrade, Nucl. Fusion 53 (7) (2013).
[16] R. Yan, J. Peng, R. Ding, et al., Surface recovery of the CXRS first mirror of EAST, IEEE Trans. Plasma Sci. 47 (4) (2019) 1769–1773.
[17] M. Rubel, G. Temmerman, J. Coad, et al., Mirror test for international thermonuclear experimental reactor at the JET tokamak: an overview of the program, Rev. Sci. Instrum. 77 (2006) 06F525.
[18] Y. Zhou, B. Gao, Y. Jiao, et al., Study of first mirror exposure and protection in HL-2A tokamak, Fusion Eng. Des. 81 (23–24) (2006) 2823–2826.
[19] M.F.M. De Bock, R. Barnsley, et al., ITER perspective on fusion reactor diagnostics—a spectroscopic view, J. Instrum. 11 (2016) P08010.
[20] C. Guillon, S. Vives, M. Aumeunier, et al., Final design and tests of the in-vessel shutter of the ITER wide angle viewing system (WAVS) in equatorial port 12, IEEE Trans. Plasma Sci. (2024).
[21] L. Marot, C. Linsmeier, B. Eren, et al., Can aluminium or magnesium be a surrogate forberyllium: A critical investigation of their chemistry, Fusion Eng. Des. 88 (9–10) (2013) 1718–1721.
[22] C.X. Wang, R. Yan, Y.M. Liu, et al., Cleaning of two mirrors in the first mirror unit using radiofrequency capacitively coupled plasma, Plasma Sci. Technol 26 (9) (2024).
[23] L. Moser, L. Marot, B. Eren, et al., Towards plasma cleaning of ITER first mirrors, Nucl. Fusion 55 (2015) 063020.
[24] L. Moser, L. Marot, R. Steiner, et al., Plasma cleaning of beryllium coated mirrors, Phys. Scr. T167 (2016) 014069.
[25] M. Yaala, L. Moser, R. Steiner, et al., Deuterium as a cleaning gas for ITER first mirrors: experimental study on beryllium deposits from laboratory and JET-ILW, Nucl. Fusion 59 (2019) 096001.
[26] L. Dittrich, P. Petersson, H. Laabadi, et al., Impact of ion irradiation and film deposition on optical and fuel retention properties of Mo polycrystalline and single crystal mirrors, Nucl. Mater. Energy 37 (2023).
[27] W. Zheng, R. Yan, G. Zuo, et al., Effect of lithium on the atmospheric corrosion characteristics of TZM as the first-wall material in EAST, J. Nucl. Mater. 594 (2024).
[28] Y. Cheng, L. Zhang, A. Hu, et al., Experimental study on metallic impurity behavior with boronization wall conditioning in EAST tokamak, Nucl. Mater. Energy 41 (2024) 101744.
[29] J.H. Wu, J.S. Hu, Y. Chen, et al., Recent results of boronization on EAST and HT-7 superconducting tokamak, J. Nucl. Mater. 415 (1) (2011) S1046–S1049.
[30] J.G. Li, Y.P. Zhao, X.M. Gu, et al., ICRF boronization – a new technique towards high efficiency wall coating for superconducting tokamak reactors, Nucl. Fusion 39 (1999) 973.
[31] A. Litnovsky, Y. Krasikov, V. Kotov, et al., Mirror station for studies of the protection of diagnostic mirrors from impurity contamination in ITER: design and first results, Fusion Eng. Des. 96 (2015) 290–293.
[32] C. Vorpahl, A. Alekseev, S. Arshad, et al., ITER diagnostic shutters, Fusion Eng. Des. 123 (2017) 712–716.
[33] F. Ding, G.N. Luo, R.A. Pitts, et al., Overview of plasma–material interaction experiments on EAST employing MAPES, J. Nucl. Mater. 455 (1–3) (2014) 710–716.
[34] A. Garcia-Carrasco, P. Petersson, M. Rubel, et al., Plasma impact on diagnostic mirrors in JET, Nucl. Mater. Energy 12 (2017) 506–512.
[35] Y.H. Guan, G.Z. Zuo, W. Xu, et al., First result of boronization assisted by the ICWC on EAST with full metal wall, Nucl. Fusion 65 (2025) 096020.
[36] W. Zheng, R. Yan, R. Ding, et al., Studies of material deposition on the graphite divertor tile after the 2019 experimental campaign in EAST, Nucl. Mater. Energy 33 (2022) 101252.
[37] G. De Temmerman, M.J. Baldwin, R.P. Doerner, et al., Beryllium deposition on international thermonuclear experimental reactor first mirrors: layer morphology and influence on mirror reflectivity, J. Appl. Phys. 102 (8) (2007).
[38] M. Mayer, S. An, T. Bräuer, et al., Surface loss probabilities of boron-hydride radicals in W7-X and ASDEX Upgrade, Nucl. Mater. Energy 2025 (2025) 102015.
[39] V. Kotov, D. Reiter, S. Kukushkin, et al., Numerical estimates of the ITER first mirrors degradation due to atomic fluxes, Fusion Eng. Des. 86 (2011) 1583.
[40] K. Kogut, N. Trifonov, V. Kurnaev, Modeling of the first mirror surface composition under ITER relevant particle irradiation, J. Nucl. Mater. 438 (2013) S731–S734.
[41] S.H. Hong, E. Bang, S. Son, et al., First mirror deposition/erosion experiment by using multi-purpose manipulators in KSTAR, Fusion Eng. Des. 109–111 (2016) 426–431.
[42] L. Marot, E. Meyer, M. Rubel, et al., Performances of Rh and Mo mirrors under JET exposure, J. Nucl. Mater. 438 (2013) S1187–S1191.